Hydrodynamics of Suspensions Agitated by Pitched-Blade Turbine

Michael Pettersson and Åke C. Rasmuson
Dept. of Chemical Engineering and Technology, Royal Institute of Technology, S-100 44 Stockholm, Sweden

The complete local fluid velocity vector was determined by three-dimensional phase-Doppler anemometry, while the velocity vector of suspended process particles was being measured. Three-dimensional mean and fluctuating velocities, complete Reynolds stresses, 3-D length macroscales, and turbulent energy dissipation rates are presented. The difference in mean and fluctuating velocities of the process particles and the fluid is also examined. Tangential mean flow opposite to the impeller rotation is observed at certain locations just outside and above the impeller, and impeller fluctuations are found also in the inflow to the impeller. The outflow of the impeller exhibits strong spatial variations. Length macroscales are essentially independent of impeller speed, but vary significantly in the tank. Local energy dissipation rates increase with agitation rate raised to power three. Differences in mean and fluctuating velocities of the two phases are normally small, but increase in the discharge flow, where differences in the direction are also observed.

Introduction

Fluid mixing is of central importance in many production systems within chemical and process industries, and solids suspending is probably the most common mixing operation. An industrial plant for production of fine chemicals and pharmaceuticals comprises a significant number of agitated vessels, applied for different process steps like blending, chemical reaction, extraction, and crystallization. The hydrodynamics in agitated vessels are very complex. The fluid flow is usually highly turbulent and varies significantly both in magnitude and direction within the tank. The periodic action of the impeller blades and the recirculating flow in the tank further add to the complexity. At present, process design is usually based on laboratory or pilot-plant experiments from which scaling up is performed. Even full-scale experimentation is sometimes used to develop the process. An improved control and design of agitated vessel processes demand a more detailed description and understanding of the local conditions. Considerable work has been performed on the minimum suspending stirring rate, but the local hydrodynamic conditions in an agitated suspension is not often studied.

The Rushton turbine is used in most studies on stirred tank hydrodynamics (Günkel and Weber, 1975; Wu and Patterson, 1989; Stoots and Calabrese, 1995). For flow-dependent processes, such as solids suspending, pitched blade turbines (PBT) are more useful. However, for this type of agitator less information can be found. Except for mean and fluctuating velocities, few data on turbulence parameters have been reported. The influence of impeller geometry (Jaworski et al., 1988; Ranade and Joshi, 1989) and impeller clearance (Jaworski et al., 1991; Ranade and Joshi, 1989) on mean and fluctuating velocities have been experimentally investigated. The flow pattern for Newtonian and non-Newtonian fluids (Nouri and Whitelaw, 1990), the Power number (Bates et al., 1963; Rewatkar et al., 1990; Shiue and Wong, 1984) and the mixing time (Raghav Rao and Joshi, 1988; Rewatkar and Joshi, 1991) have been presented. Fluctuating velocities, sometimes in terms of turbulence intensity or turbulent kinetic energy, have been estimated (Jaworski et al., 1988, 1991; Ranade and Joshi, 1989; Ranade et al., 1992). Kresta and Wood (1993a) present some data on turbulent kinetic energy, Reynolds stresses, time macroscales, and local energy dissipation rates. Using an integral kinetic energy balance over a control volume, Fort et al. (1971) and Jaworski and Fort (1991) calculated average energy dissipation rates. The trailing vortex leaving the impeller blade has been studied (Tatterson et al., 1981; Ali et al., 1981).

Correspondence concerning this article should be addressed to Å. C. Rasmuson.

Two velocity components are determined simultaneously by Armstrong and Ruszkowski (1988), Bakker and van den Akker (1994), and Mahouast et al. (1989). 3-D velocity vectors in stirred tanks are occasionally presented (Ranade and Joshi, 1989; Wu and Patterson, 1989; Stoots and Calabrese, 1995) but are obtained by repeated 1-D or 2-D measurements. Of these, only Bakker and van den Akker (1994) and Ranade and Joshi (1989) studied a PBT. In only one old study (Ito et al., 1975) the 3-D velocity vector was *directly* determined by electrochemical probes. Besides from an old study (Kuboi et al., 1974) in which a photographic technique was used, only one recent study has been done where the fluid flow and the velocity of suspended particles are measured simultaneously. Guiraud et al. (1993) used a 1-D phase-Doppler anemometer (PDA) to measure axial and radial mean velocities of both phases.

In the present work, a 3-D phase-Doppler anemometer is applied to investigate the conditions in a suspension agitated by a pitched-blade turbine. For the first time in agitated tanks (besides the work of Ito et al., 1975), the complete 3-D velocity vector of the fluid is directly determined. In addition, the 3-D velocity of suspended particles (0.06 vol. %) is recorded, simultaneously. Measurements are performed at different agitation rates, in four different horizontal planes and at different radial and tangential locations. Fluid mean and fluctuating velocities, the complete Reynolds stress tensor, macroscales of turbulence, energy dissipation rates, and the difference in mean and fluctuating velocities of the two phases are reported. The objective is to provide a first set of data comprising a complete characterization of the suspension flow at each location. The data contribute to an increased understanding of the conditions in agitated suspensions and can be used for validation of computer simulations.

Experimental Studies

Phase-Doppler anemometer

The phase-Doppler system is a six-beam, fiber based, three-component system (Dantec Measurement Technology) utilizing the green (514.5 nm), blue (488.0 nm) and violet (476.5 nm) lines of an Ar-ion laser (Spectra Physics 2020). The principles of the technique are described by Baukhage (1988). The two green laser beams intersect to form an interference pattern shaped like a strongly elongated spheroid called probe volume. From the light scattered by particles traversing the interference pattern, the local, instantaneous velocity vector perpendicular to the interference pattern can be determined. Two blue laser beams from the same probe (2-D) generate a second interference pattern that overlaps the green probe volume, however, it is rotated 90°. This allows for determination of a second orthogonal velocity component. The two violet beams from a separate probe (1-D) at a 90° angle to the first generate a third interference pattern perpendicular to the previous two. For particles traversing the volume in common to all three probe volumes called the measurement volume (approximately 0.003 mm^3), the complete 3-D velocity vector can be determined. The green light is used to determine the size of spherical particles. Scattered green and blue light is collected by a receiver. The angle between the optical axis of the receiving optics relative to direct forward scattering of the green and the blue light is approximately 69°, assuring that size estimation is predominantly based on reflected light. Scattered violet light is collected by the 2-D probe. Data for the transmitting and the receiving optics are given in Table 1. The system is described in more detail by Pettersson (1996), where also validation is reported, and methods of data evaluation are analyzed.

Table 1. Parameters of the Transmitting and Receiving Optics

Wavelength (nm)	514.5	488	476.5
Focal length (mm)	600	600	600
Beam intersection angle (deg)	6.86	6.86	6.86
Beam expansion	1.85	1.85	1.85
Fringe spacing (μm)	4.30	4.08	3.98
Number of fringes	37	37	37
Volume length (mm)	3.51	3.33	3.25
Volume height (mm)	0.158	0.149	0.146
Volume width (mm)	0.157	0.149	0.146
Scattering angle effective (deg)	68.5 (74.1)		
Angle adjustment (mm)	0.3		
Focal length (mm)	600		
Polarization (deg)	90		
Maximum particle size (μm)	515.4		
Phase factor U1-U2 (deg/μm)	1.3915		
Phase factor U1-U3 (deg/μm)	0.5027		
Scattering mode	Reflection		

Stirred tank

The experiments are performed in a flat bottomed, cylindrical glass vessel filled with approximately 7 L of deionized water. The water has been filtrated twice through filters with a pore size of 3 and 0.2 μm, respectively. The vessel is provided with four equally spaced baffles made of stainless steel. The agitator is a 45° pitched, four-blade turbine ($D_i/D_t = 0.4$) pumping downwards. The dimensions of the vessel and the impeller are given in Figure 1. The cylindrical vessel is placed

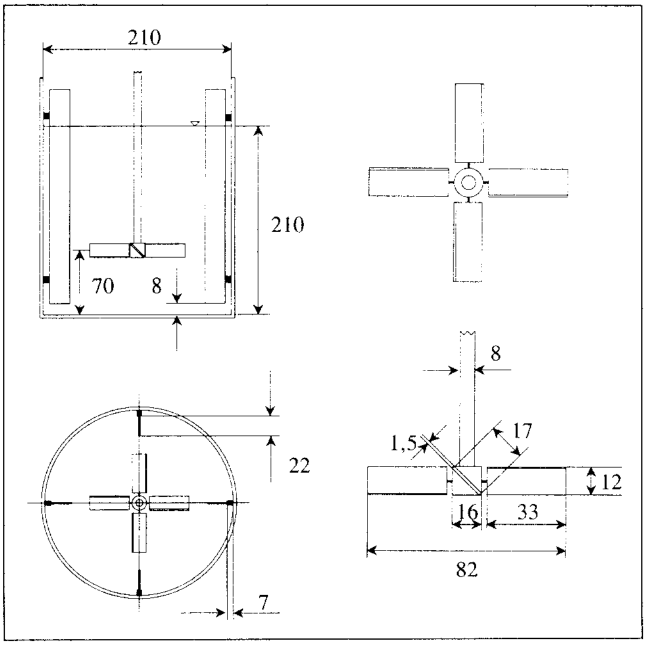

Figure 1. Vessel and the impeller (mm).

inside a squared glass tank filled with water in order to reduce distortion of the laser beams at the cylindrical vessel wall (Pettersson, 1996). The vessels are placed on a milling table that together with the pillar of an upright drill serves as a 3-D mechanical positioning system. The accuracy in the positioning is approximately 0.05 mm in the horizontal plane and 0.5 mm in the vertical direction. By turning the set of baffles inside the vessel, the tangential location of the measurement point is altered. The walls of the squared glass tank are perpendicular to the optical axes of the 2-D and the 1-D probes, respectively, and the optical axis of the 2-D probe is always through the center of the cylindrical tank.

Particles

Two types of particles are added to the fluid. Spherical metallic coated glass particles (TSI GmbH) with a specified density of 2.6 g/cm^3 and a number mean size of 4 μm are used as fluid tracers. Electrosensing zone measurements (Elzone 180 XY) determine the number mean diameter of these particles to 6.9 μm and the corresponding geometric standard deviation to 1.9. Glass beads with a high degree of sphericity (Duke Scientific Corp.) are used to simulate process particles. The glass beads are normal distributed in size, have a mean size of 321 ± 9.6 μm, and a standard deviation of 13.2 μm. The density is 2.42 g/cm^3. The two types of particles are denoted seed particles and process particles, respectively. 0.10 g of seed particles is added to the fluid, and the concentration of process particles is 0.06% by volume.

Experiments

Measurements are performed at four different horizontal planes in the tank, shown in Figure 2. The origin of coordinates is at the center of the impeller hub, where h is defined positive upwards, r towards the vessel wall, and ξ in the direction of impeller rotation. The corresponding velocity components u_h, u_r and u_ξ are defined likewise. The measurements are carried out at three different impeller speeds: 450, 525 and 600 rpm. The conditions are turbulent since the impeller Reynolds number ranges from 5.0×10^4 to 6.7×10^4. The mean power input to the liquid varies by a factor 2.4. In the baffle region at $h = -10$ mm five different impeller speeds have been studied: 420, 450, 500, 550, and 600 rpm. From visual observations, it is concluded that the minimum impeller speed required to suspend the process particles is approximately 450 rpm. This is 8% higher than the value obtained by the Zwietering equation (Zwietering, 1958), using the S value for a propeller. The results for the fluid and the process particles are based on particles recorded in the range 5–21 μm and 200–500 μm, respectively. Between $1.5 \cdot 10^5$ and $3 \cdot 10^5$ data values (particles) are collected in each experiment (one location and one impeller speed) at a data rate of 100–500 Hz. Approximately 50% of the measured particles are within the range 5–21 μm, and between 0.5 and 3% are within the range 200–500 μm. The statistical error in mean velocity $\Delta\overline{u_i}$ ranges from 0.0004 to 0.004 m/s for the seeding particles, and from 0.002 to 0.02 m/s for the process particles. The relative error in fluctuating velocity $(\Delta u'_{i,\mathrm{rms}}/u'_{i,\mathrm{rms}})$ ranges from 0.3 to 0.8% for the fluid, and from 1.1 to 5.5% for the process particles.

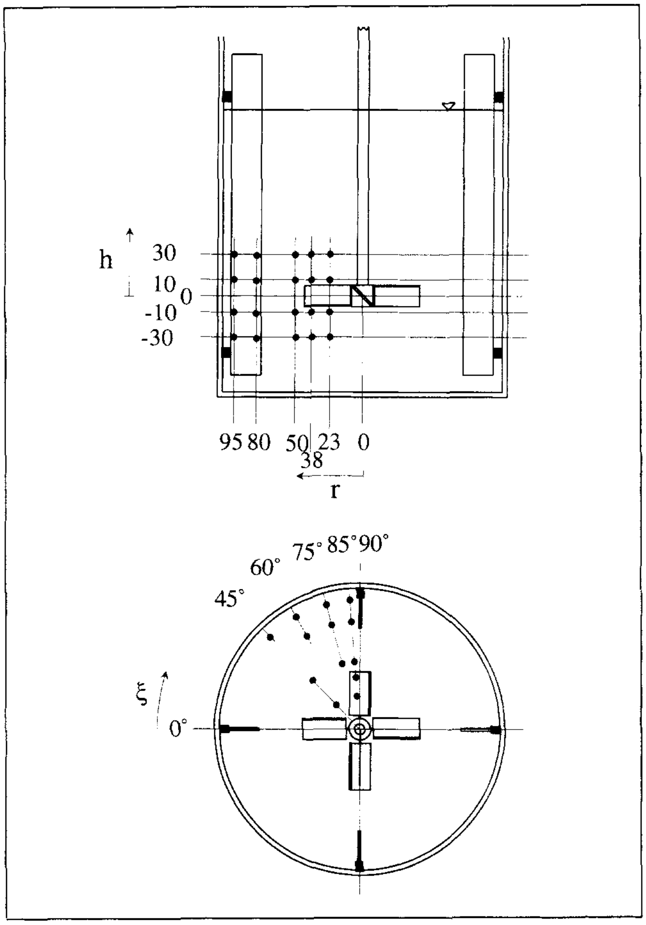

Figure 2. Location of measurement points.

Results

Local 3-D mean and fluctuating velocities of fluid and of suspended process particles are estimated. Reynolds stresses, macroscales of turbulence and turbulent energy dissipation rates are evaluated for the fluid. The mean and fluctuating velocities of the process particles are compared with those of the fluid. Unless specified, the results are corrected for velocity bias using the instantaneous 3-D velocity (Pettersson, 1996). Locations at $h = \pm 10$ mm and $r = 23$ and 38 mm will be referred to as the impeller region. The baffle region denotes locations at $r = 80$ and 95 mm. Measurement points below the impeller at $r = 23$ and 38 mm are referred to as the discharge flow.

Mean velocity

The bias corrected components of the mean velocity are calculated as

$$\overline{u_i} = \frac{\sum\limits_{n=1}^{N_{\mathrm{part}}} (u_i/U)_n}{\sum\limits_{n=1}^{N_{\mathrm{part}}} (1/U)_n} \tag{1}$$

Figure 3 shows the projection of the 3-D mean velocity vector in a vertical plane through the center of the tank (left) and in

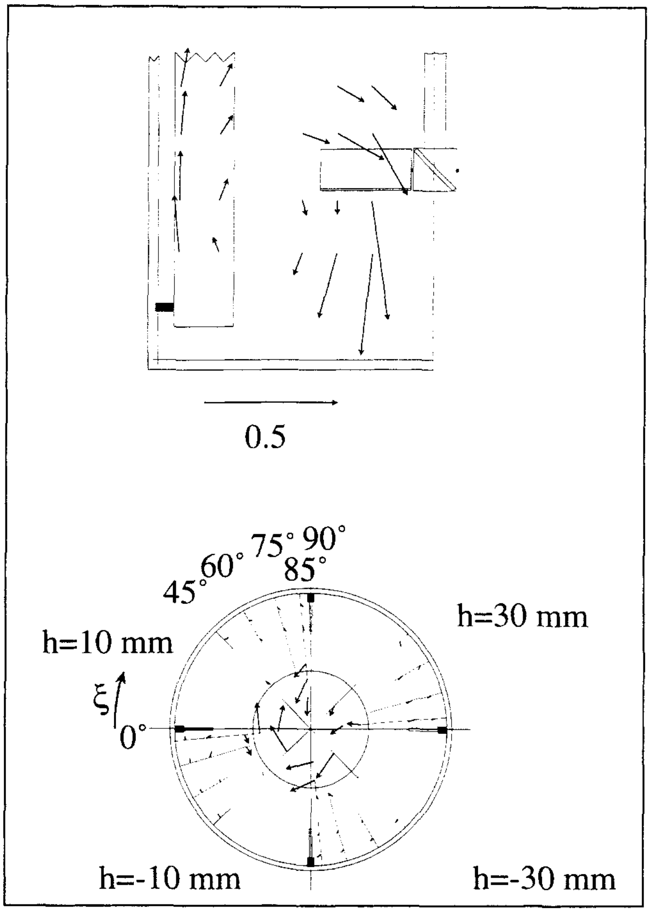

Figure 3. Projection of 3-D mean velocity vectors in the axial-radial plane $\xi = 85°$ (left) and the radial-tangential plane (right).

Normalized by the impeller tip speed: πND_i.

horizontal planes (right). In the figure to the right, each quadrant gives results for a certain horizontal plane. The overall flow pattern is as expected, but the flow around the impeller is more complex. In the discharge flow, the axial and tangential velocities are strong but the radial component is negligible. The maximum axial and tangential velocities are obtained in this region and are $0.44 \times U_{\text{tip}}$ and $0.24 \times U_{\text{tip}}$, respectively. Moving in a radial direction (m) along the impeller blade from $r = 23$ to $r = 38$ mm at $h = -10$ mm, the axial mean velocity decreases significantly while the tangential component slightly increases, resulting in a change in flow direction. The strong radial variation below the impeller agrees with the results of Kresta and Wood (1993b), and with the description of a liquid jet coming out from the impeller. At $h = -30$ mm, the radial variation is less. In the impeller region below the impeller, there is a significant tangential component in the same direction as the impeller rotation. However, just outside the impeller ($r = 50$ mm) at $h = -10$ mm and $\xi = 75°$ and 85°, the tangential mean flow component is in the opposite direction to the impeller rotation, but the mean velocity is low and the fluctuations are quite high. At $\xi = 45°$, the mean velocity is very low but in the same direction as the impeller rotation. Also, above the impeller at $h = 10$ mm, $\xi = 85°$, and $r = 23$, 38, and 50 mm the mean velocity vector is opposite to the rotation direction, while the tangential flow is less uniform at $h = 30$ mm. Obviously, the baffle influences on the flow in the impeller region, and this is also observed by Kresta and Wood (1993b). The radial component is quite strong at all locations in the impeller region above the impeller, showing how liquid is drawn towards the center. The baffle region, especially at $r = 95$ mm, is dominated by the axial component. At $r = 95$ mm, the axial mean velocity decreases slightly when moving closer to the baffle, except for at $h = -30$ mm.

The magnitudes of the three fluid mean velocity components $\overline{u_h}$, $\overline{u_\xi}$ and $\overline{u_r}$ are proportional to the impeller tip speed πND_i, which agrees with earlier work (Fort et al., 1971; Jaworski et al., 1988; Kresta and Wood, 1993b; Ranade and Joshi, 1989). The flow angle formed by the axial and radial mean velocity components in the discharge flow do not vary with impeller Reynolds number. However, the range studied is quite limited compared to that of Nouri and Whitelaw (1990). Our results do not indicate changes in the flow pattern within the range of Reynolds numbers studied.

The magnitude of the 3-D mean velocity (m/s)

$$\overline{U} = \sqrt{\overline{u_h}^2 + \overline{u_r}^2 + \overline{u_\xi}^2} \tag{2}$$

is shown in Figure 4, normalized by the impeller tip speed. The mean velocity is at a maximum at $r = 23$ mm and decreases with increasing radial distance up to $r = 80$ mm with minor differences between $r = 50$ and $r = 80$ mm. In the baffle region there is again a clear increase toward the vessel wall, showing that the upflow stream along the wall is quite thin. An increase is observed in $\overline{U}$, from $h = -10$ to $h = -30$ mm at $r = 38$ mm illustrating how the rather narrow jet leaving the impeller close to the center gradually spreads out. Alternatively, it may suggest that the discharge flow is an accelerating flow as proposed by Ranade and Joshi (1989). In comparison to the change in $\overline{U}$ with radial distance, the dependence on tangential direction is much lower. Axial velocity gradients are strongest in the region above and below the impeller. Close to the vessel wall, $r = 95$ mm, there is a small reduction in $\overline{U}$ with increasing distance from the bottom of the vessel.

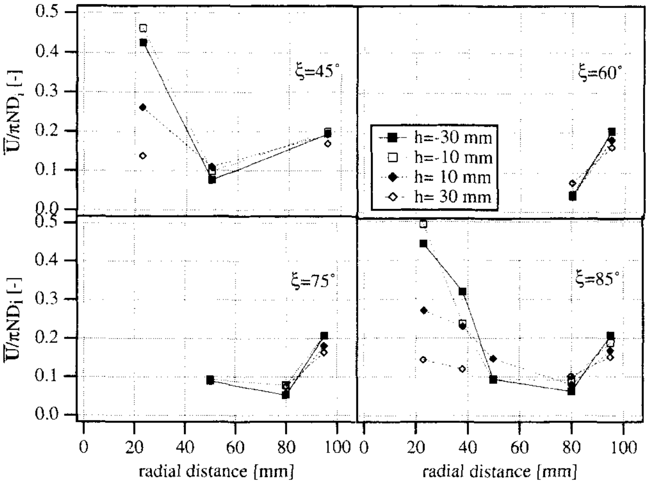

Figure 4. Normalized 3-D fluid mean velocity, $N = 450$ rpm.

Fluctuating velocity

The root-mean-square (rms) of the total fluctuating velocity is calculated by

$$\sqrt{\overline{(u_i')^2}} = \sqrt{\frac{\sum_{n=1}^{N_{\text{part}}} [(u_i)_n - \overline{u_i}]^2 \cdot (1/U)_n}{\sum_{n=1}^{N_{\text{part}}} (1/U)_n}} \qquad (3)$$

All three components of the fluctuating velocity vector scale with impeller speed and this agrees with previous findings concerning the radial and axial rms fluctuating velocities (Jaworski et al., 1988; Ranade and Joshi, 1989). Figure 5 shows the rms value of the total fluctuating velocities at $h = -10$ mm, normalized by impeller tip speed. Except for at $r = 23$ mm and 38 mm, the fluctuations are roughly equal in all three directions, but vary significantly with radial direction. The highest fluctuations are found at the tip of the impeller. Axial variations are found in the impeller region (higher fluctuations below the impeller), but are low in the baffle region. In the baffle region, the difference between the three fluctuating velocity components decreases towards the bottom.

In the impeller region, the total fluctuating velocity includes a periodic contribution from the impeller blades. This periodic fluctuation is superimposed on the true turbulent fluctuation (van't Riet et al., 1976)

$$u'_{\text{tot}}(t) = u'_{\text{turb}}(t) + u'_{\text{per}}(t) \qquad (4)$$

The periodic part can be estimated by the autocorrelation function. If there is no correlation between random and periodic turbulence, the autocorrelation function can be expressed as (Wu and Patterson, 1989)

$$\overline{u'(t)\cdot u'(t+\tau)}_{\text{tot}} = \overline{u'(t)\cdot u'(t+\tau)}_{\text{turb}} + \overline{u'(t)\cdot u'(t+\tau)}_{\text{per}} \qquad (5)$$

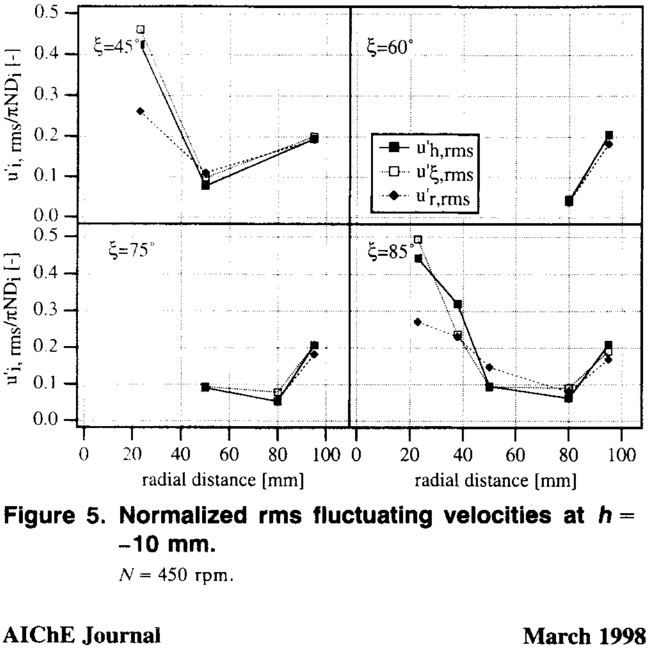

Figure 5. Normalized rms fluctuating velocities at $h = -10$ mm.

$N = 450$ rpm.

As τ goes to infinity, the term representing the contribution from the random turbulence approaches zero, and only the periodic contribution remains. The periodic contribution is calculated by fitting Eq. 6 to the experimental autocorrelation function in the range $1 \leq \tau \leq 2$ s.

$$\overline{u'(t)\cdot u'(t+\tau)}_{\text{per}} = a_0 \cdot \cos(a_1 \cdot \tau) + a_2 \cdot \cos(2a_1 \cdot \tau) \qquad (6)$$

At $\tau = 0$, Eqs. 5 and 6 reduce to

$$\overline{u'(t)^2}_{\text{tot}} = \overline{u'(t)^2}_{\text{turb}} + \overline{u'(t)^2}_{\text{per}} \qquad (7)$$

$$\overline{u'(t)^2}_{\text{per}} = a_0 + a_2 \qquad (8)$$

and consequently the turbulent fluctuation can be calculated from the determination of the total fluctuation. A periodic fluctuation can be detected at $r = 23$ and 38 mm in the planes $h = -30$, -10 and 10 mm, that is, the impeller affects the fluctuating velocity also above the impeller. Total rms values are compared in Table 2 with those of the random and the periodic fluctuations as estimated by the procedure described. In the impeller region, the difference between the components of the random rms velocity is less than the difference between the components of the total rms velocity. However, at least for the horizontal plane $h = -10$ mm in the discharge flow, the differences between the components are still significant. The 1-D intensity of turbulence u_i'/u_i, calculated from random fluctuations only, varies considerably with direction. Intensities of turbulence of several thousands of percent are found when the mean velocity is low. Based on random fluctuations only, results on the turbulent kinetic energy q (m^2/s^2) and the 3-D intensity of turbulence $\boldsymbol{Tu}$ (Calabrese and Stoots, 1989)

$$\boldsymbol{Tu} = \frac{\sqrt{2\cdot q}}{\overline{U}} = \frac{\sqrt{(u'_{h,\text{rms turb}})^2 + (u'_{\xi,\text{rms turb}})^2 + (u'_{r,\text{rms turb}})^2}}{\overline{U}} \qquad (9)$$

are shown in Figures 6 and 7. The turbulent kinetic energy is particularly high in the discharge region especially close to the impeller tip. It may be noticed that the maximum mean velocity is obtained at $r = 23$ mm (Figure 4), while the maximum turbulence is obtained at $r = 38$ mm (Figure 6). The 3-D intensity of turbulence receives values of several hundred percent at low mean velocities. The decrease in $\boldsymbol{Tu}$ at $r = 80$ mm as ξ is increased from 60° to 85° is related to the increase in $\overline{u_h}$ towards the baffle.

Reynolds stresses

The Reynolds stresses are calculated by Eq. 10, based on the total velocity fluctuation defined in Eq. 4.

$$\overline{u_i' \cdot u_j'} = \frac{\sum_{i=1}^{N_{\text{part}}} u_i' \cdot u_j'/U}{\sum_{i=1}^{N_{\text{part}}} 1/U} \qquad (10)$$

Table 2. Total, Periodic and Turbulent Fluctuating Velocities

Location	N	$u_{\mathrm{tot}}/U_{\mathrm{tip}}$	$u'_{\mathrm{per}}/U_{\mathrm{tip}}$	$u'_{\mathrm{turb}}/U_{\mathrm{tip}}$	$v'_{\mathrm{tot}}/U_{\mathrm{tip}}$	$v'_{\mathrm{per}}/U_{\mathrm{tip}}$	$v'_{\mathrm{turb}}/U_{\mathrm{tip}}$	$w'_{\mathrm{tot}}/U_{\mathrm{tip}}$	$w'_{\mathrm{per}}/U_{\mathrm{tip}}$	$w'_{\mathrm{turb}}/U_{\mathrm{tip}}$
103885	464	0.0885	0.0379	0.0800	0.1087	0.0320	0.1039	0.0714	0.0226	0.0677
hr ξ	534	0.0897	0.0358	0.0823	0.1140	0.0306	0.1098	0.0763	0.0227	0.0728
	608	0.0867	0.0276	0.0822	0.1126	0.0243	0.1100	0.0750	0.0178	0.0728
102345	456	0.0689	0.0448	0.0523	0.1180	0.0521	0.1059	0.0776	0.0189	0.0752
	534	0.0689	0.0408	0.0556	0.1147	0.0467	0.1048	0.0785	0.0179	0.0764
	602	0.0679	0.0374	0.0566	0.1123	0.0428	0.1038	0.0784	0.0162	0.0767
102385	461	0.0707	0.0432	0.0560	0.1206	0.0525	0.1085	0.0941	0.0204	0.0919
	530	0.0719	0.0343	0.0632	0.1200	0.0396	0.1133	0.0958	0.0134	0.0948
	603	0.0690	0.0310	0.0617	0.1151	0.0369	0.1090	0.0951	0.0121	0.0943
−103885	454	0.2358	0.0983	0.2144	0.2843	0.0943	0.2682	0.2422	0.1242	0.2079
	527	0.2446	0.0868	0.2286	0.2865	0.0778	0.2757	0.2442	0.1044	0.2208
	602	0.2469	0.0675	0.2375	0.2832	0.0711	0.2741	0.2458	0.0844	0.2308
−102345	454	0.1386	0.0431	0.1317	0.1482	0.0000	0.1482	0.1716	0.0833	0.1500
	530	0.1393	0.0449	0.1319	0.1498	0.0000	0.1498	0.1707	0.0816	0.1499
	604	0.1404	0.0449	0.1330	0.1495	0.0000	0.1495	0.1673	0.0783	0.1479
−102385	457	0.1394	0.0476	0.1310	0.1433	0.0447	0.1361	0.1876	0.1078	0.1535
	529	0.1418	0.0457	0.1343	0.1607	0.0484	0.1533	0.1979	0.1059	0.1672
	600	0.1434	0.0391	0.1380	0.1592	0.0387	0.1544	0.1908	0.0866	0.1700
−303885	455	0.1535	0.0292	0.1507	0.1509	0.0439	0.1444	0.1481	0.0365	0.1436
	526	0.1522	0.0273	0.1498	0.1456	0.0359	0.1412	0.1458	0.0327	0.1421
	600	0.1511	0.0237	0.1492	0.1356	0.0253	0.1333	0.1465	0.0278	0.1438
−302345	454	0.1300	0.0079	0.1298	0.1274	0.0373	0.1218	0.1204	0.0378	0.1143
	529	0.1301	0.0084	0.1298	0.1229	0.0282	0.1196	0.1199	0.0323	0.1155
	600	0.1295	0.0108	0.1291	0.1155	0.0231	0.1132	0.1189	0.0304	0.1150
−302385	452	0.1291	0.0167	0.1281	0.1293	0.0191	0.1279	0.1266	0.0392	0.1204
	528	0.1291	0.0174	0.1279	0.1265	0.0160	0.1255	0.1249	0.0349	0.1199
	600	0.1272	0.0169	0.1261	0.1198	0.0132	0.1191	0.1257	0.0359	0.1204

Results are presented in Figure 8. The Reynolds stresses are found to be proportional to the impeller tip speed squared, which is to be expected at least for the normal stresses. The variation in radial and axial direction are strong, but the dependence on tangential location is very low. As expected, the normal stresses are in general larger than the shear stresses, especially below the impeller. Above the impeller and even more so in the baffle region, the differences are much smaller. In the baffle region, where the periodic contribution is negligible, the shear stresses are very close to zero. For estimation of true Reynolds stresses, the periodic action of the impeller blades in the vicinity of the impeller should be accounted for (Mahouast et al., 1989). Cross-correlation functions $\overline{u'_i(t)\times u'_j(t+\tau)}$ at $\tau=0$ are identical to the shear stresses. Complete cross-correlation function curves have been calculated for one measurement at $h=-10$ mm, $r=38$ mm, $\xi=85°$, where the shear stresses are the largest. No periodicity is found in $\overline{u'_r(t)\times u'_\xi(t+\tau)}$, but a clear periodic behavior with a decreasing amplitude is found for $\overline{u'_h(t)\times u'_\xi(t+\tau)}$

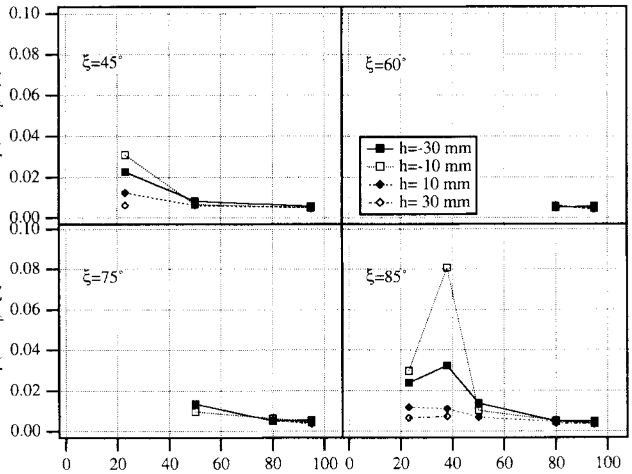

Figure 6. Normalized turbulent kinetic energy.
$N=450$ rpm.

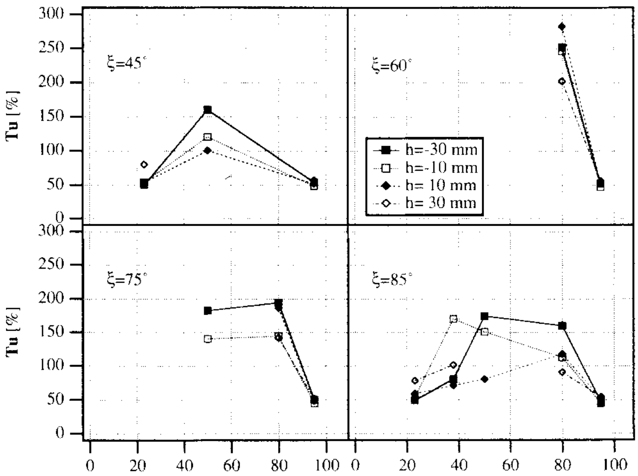

Figure 7. 3-D intensity of turbulence, $N=450$ rpm.

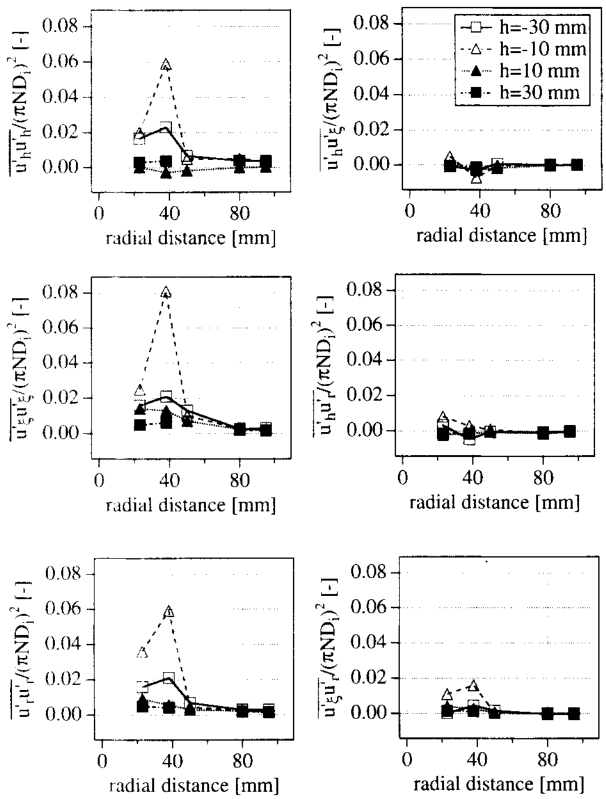

Figure 8. Normalized Reynolds stresses.

$N = 450$ rpm; $\xi = 85°$.

and $\overline{u_h'(t)\times u_r'(t+\tau)}$. The autocorrelation function $\overline{u_i'(t)\times u_i'(t+\tau)}$, and thereby the normal stresses, can be corrected for the periodic action of the impeller blades as shown in Eqs. 5 to 8. Assuming that the same scheme is applicable also to a cross-correlation function, the results of Table 3 are obtained. Depending on whether the shear stresses are positive or negative, they either decrease or increase at the correction for periodicity. Unfortunately, calculations in order to correct for periodicity become very tedious, and this problem is handled better directly by angle-resolved measurements.

Table 3. Total, Periodic and Turbulent Components of the Shear Stresses at $h = -10$ mm, $r = 38$ mm, $\xi = 85°$, $N = 600$ rpm

Component	Total	Periodic	Turbulent
$\overline{u_h'u_\xi'}$	−0.0446	0.0344	−0.0790
$\overline{u_h'u_r'}$	0.0209	0.0198	0.0011
$\overline{u_r'u_\xi'}$	0.1074	0	0.1074

Autocorrelation coefficients

The Eulerian autocorrelation coefficients $R_E(\tau)$ are calculated using the slotting technique of Mayo et al. (1974) for a maximum lag time of both 2 and 10 s using a slot width of 2 and 4 milliseconds, respectively. The shorter maximum lag time is used in estimation of time macroscales, while the larger limit is used in detection of the longer periodicities discussed below. The autocorrelation coefficient is calculated as (Pettersson, 1996)

$$R_{E,i}(\tau) = \frac{\overline{u_i'(t)\cdot u_i'(t+\tau)}_{\text{turb}}}{\overline{u_i'(t)^2}_{\text{turb}}} = \frac{\dfrac{\sum\limits_{n=1}^{N_{\text{part}}}\sum\limits_{m} u_{i,n}'\cdot u_{i,m}'/U_n}{\sum\limits_{n=1}^{Q} 1/U_n}}{\dfrac{\sum\limits_{n=1}^{N}\sum\limits_{m} u_{i,n}'\cdot u_{i,n}'/U_n}{\sum\limits_{n=1}^{N} 1/U_n}} \tag{11}$$

where

$$Q = \sum_{n=1}^{N}\sum_{m} 1 \tag{12}$$

Q is the number of fluctuating velocity products in each slot. The fluctuating velocities are determined using mean velocities corrected for velocity bias by $w_i = 1/U$. The autocorrelation coefficient is based on turbulent fluctuations only as calculated by Eqs. 4 to 8. The shape of the autocorrelation coefficient curve depends on the structure and the motion of the turbulence (Townsend, 1976). For a random velocity fluctuation, there is a monotonic decay towards zero with increasing lag time (Figure 9a). For a periodic fluctuation, the curve oscillates with a constant frequency and amplitude. However, in the present work, other behaviors also are found. Even though the data at $r = 23$ and 38 mm and $h = -30$, -10 and 10 mm are corrected for the periodic fluctuation, fluctuations having the impeller blade frequency still remain in the autocorrelation coefficients (Figure 9b). Outside this region, cases are found where the autocorrelation curve oscillates at least in one direction a few times about zero with a periodicity of one to two seconds, before finally approaching zero (Figure 9c). The amplitude of this fluctuation is always much lower than that observed at long lag times in the total fluctuation autocorrelation coefficient curves. Occasionally, autocorrelation coefficients do not reach zero until lag times of five to ten seconds (Figure 9d). When correlation over several seconds are found, these are retained when impeller speed is changed. Occasionally, some reduction is found with increasing impeller speed. In Figure 10, the measurement location is marked by a filled circle when the autocorrelation coefficient curve is not well shaped. Locations around the impeller and at $\xi = 85°$ especially exhibit complex autocorrelation coefficient curves. This is likely to relate to the complexities in the flow that is generated by the baffle as is discussed above.

Length macroscales of turbulence

Time macroscales of turbulence are calculated by integrating the autocorrelation coefficient

$$T_{E,i} = \int_0^\infty R_{E,i}(\tau)\,d\tau \tag{13}$$

A function consisting of two exponential terms is fitted to the experimental data

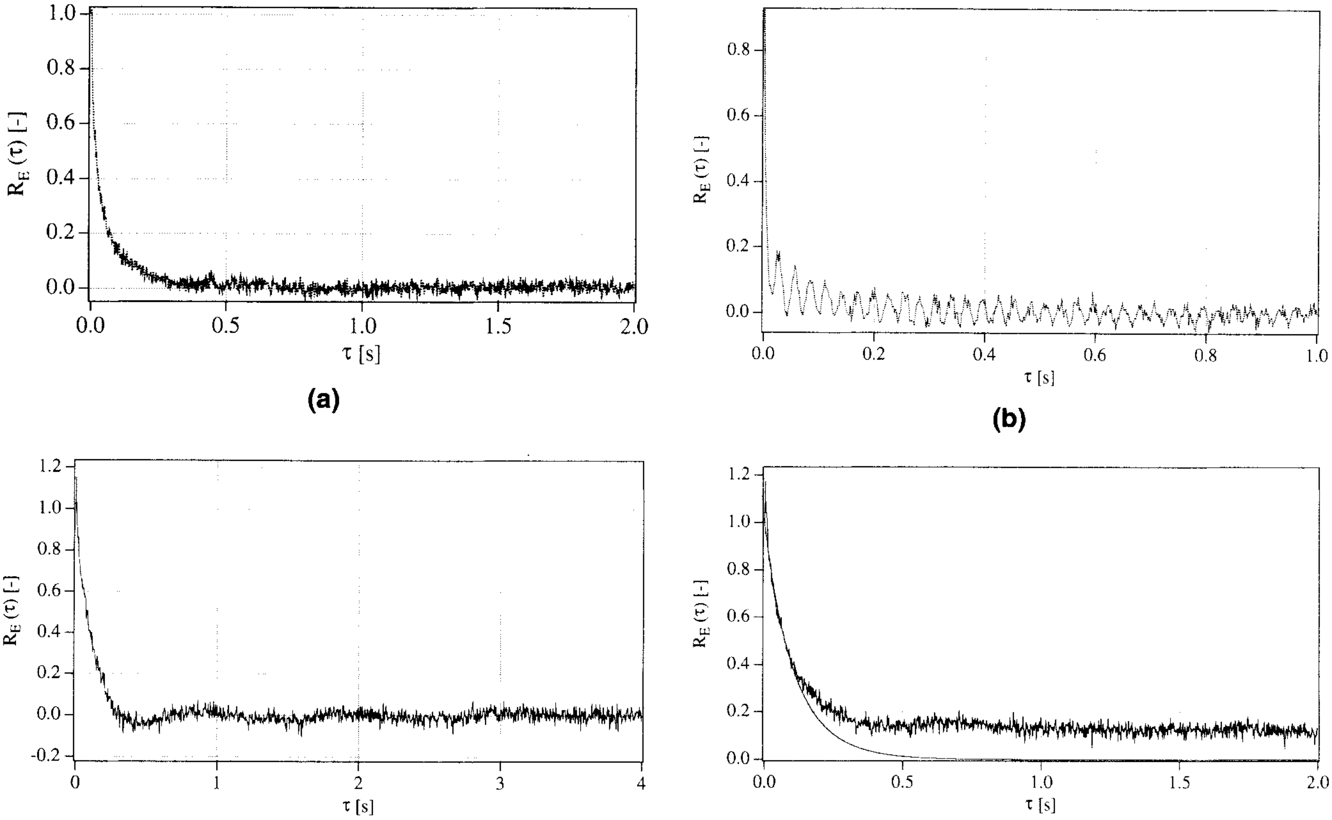

(a) **(b)** **(c)** **(d)**

Figure 9. Examples of autocorrelation coefficients.

(a) A well-behaved autocorrelation coefficient ($h = 30$ mm, $r = 95$ mm, $\xi = 45°$, $N = 450$ rpm); (b) autocorrelation coefficient with impeller blade periodicity ($h = -30$ mm, $r = 95$ mm, $\xi = 85°$, $N = 450$ rpm); (c) autocorrelation coefficient with the longer periodicity ($h = 30$ mm, $r = 80$ mm, $\xi = 85°$, $N = 450$ rpm); (d) autocorrelation coefficient not approaching zero before $\tau = 2$ s ($h = 30$ mm, $r = 80$ mm, $\xi = 85°$, $N = 450$ rpm). All are tangential components.

$$R_E(\tau) = k_1 \exp(-k_2\tau) + (1-k_1)\exp(-k_3\tau) \tag{14}$$

To obtain the time macroscale, this function is integrated between zero and infinity, unless it takes on negative values in which case the upper integration limit is taken as the time when the function becomes negative. For the cases where the autocorrelation coefficient does not reach zero until several seconds, the exponential function is fitted to a limited range of τ as shown in Figure 9d. This is assumed to be a better representation of the true random fluctuation autocorrelation coefficient. Length macroscales are obtained from the estimated time macroscales using a 3-D "convection velocity" as a proportionality factor (Wu and Patterson, 1989)

$$\Lambda_i = U_{c,i} \cdot T_{E,i} \tag{15}$$

where

$$U_{c,i}^2 = \overline{u}_i^2 \left(1 + 2\frac{\overline{u}_j^2}{\overline{u}_i^2} + 2\frac{\overline{u}_k^2}{\overline{u}_i^2} + \frac{\overline{(u_i')^2}}{\overline{u}_i^2} + 2\frac{\overline{(u_j')^2}}{\overline{u}_i^2} + 2\frac{\overline{(u_k')^2}}{\overline{u}_i^2} \right) \tag{16}$$

and indices i, j, and k denote the three velocity components. Figure 10 presents estimated values for the axial, tangential, and radial length macroscales at 450 rpm. When the autocorrelation coefficient curve is not well shaped, the macroscales should be regarded as uncertain. Obviously, the characteristic length of the eddies is not equal in the three coordinate directions. In the baffle region the macroscales vary with tangential location (Figure 11). At $r = 95$ mm, Λ_h and Λ_r increase close to the baffle while Λ_ξ decreases, the latter also found at $r = 80$ mm. Tangential variations that are larger than the estimated uncertainty are also found for the axial and tangential length macroscales at $h = -30$ mm and $r = 23$ mm. Tangential gradients arise mainly because of differences in time macroscales. In general, the time macroscale decreases and the convection velocity increases with increasing impeller speed, which results in length macroscales being independent or only weakly dependent on impeller speed. This agrees with results reported for a Rushton turbine (Wu and Patterson, 1989). The largest component macroscales are of the same size as the impeller diameter. A resultant 3-D macroscale, defined in Eq. 17 (Wu and Patterson, 1989), varies between 27 and 110 mm as shown in Figure 12.

$$\Lambda_{\text{res}} = \sqrt{\Lambda_h^2 + \Lambda_\xi^2 + \Lambda_r^2} \tag{17}$$

In the baffle region, resultant length macroscales are approximately equal to half the impeller diameter. Closer to the

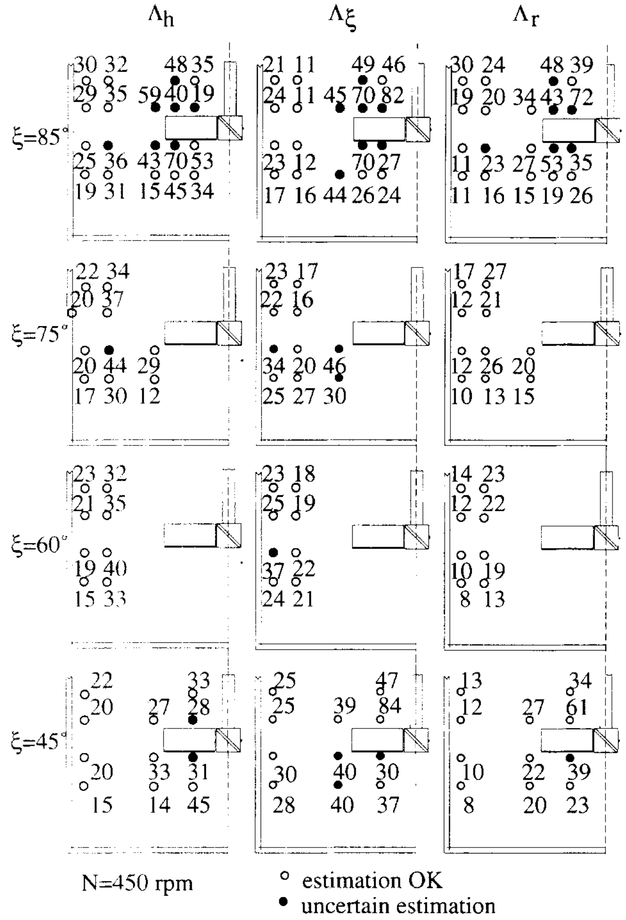

Figure 10. Length macroscales (mm).

$N = 450$ rpm.

impeller the macroscales are larger, especially in the plane just above the impeller, where resultant macroscales even exceed the diameter of the impeller.

Turbulent energy dissipation rate

The energy dissipation rate is calculated as

$$\epsilon = C_k \frac{q^{1.5}}{\Lambda_{res}} \tag{18}$$

where

$$q = \frac{1}{2}\left[(u'_{h,rms})^2 + (u'_{\xi,rms})^2 + (u'_{r,rms})^2\right] \tag{19}$$

and $C_k = 1$. The fluctuating velocities include random fluctuations only. Results are presented in Figure 13. The mean power input to the vessel $\bar{\epsilon} = P/\rho V$ is calculated using the turbulent Power number for a PBT: $N_p \approx 1.3$ (Oldshue, 1983). As expected, the highest dissipation rate is in the discharge flow leaving the impeller. Within the examined region, the maximum relative dissipation rate is approximately 6. The baffle region and the region above the impeller are characterized by small variations in dissipation rate: $\epsilon/\bar{\epsilon}$ ranges from 0.1 to 0.4. The dissipation rate decreases slightly from $r = 80$ mm to $r = 95$ mm, except for in the horizontal plane $h = -30$ mm, where a clear increase is found. In the baffle region there is also a tendency for the dissipation rate to decrease with decreasing tangential distance to the baffle. Based on all measurements where the autocorrelation coefficient curves in all three directions are well shaped, the local energy dissipation rate is found to be proportional to the agitation rate raised to power 3.18 (mean value). The standard deviation of this value is 0.25. In Figure 14 four examples are given.

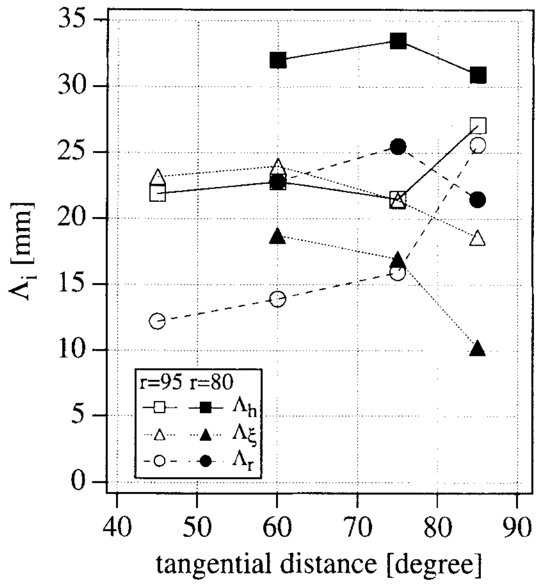

Figure 11. Length macroscales within the baffle region at $h = 30$ mm, $N = 525$ rpm, $r = 80$ mm (filled markers) and $r = 95$ mm (unfilled).

Process particle velocity

The difference in the 3-D mean velocity of the fluid and of the process particles $|\bar{U}_s - \bar{U}_p|$ is small in absolute values, nor-

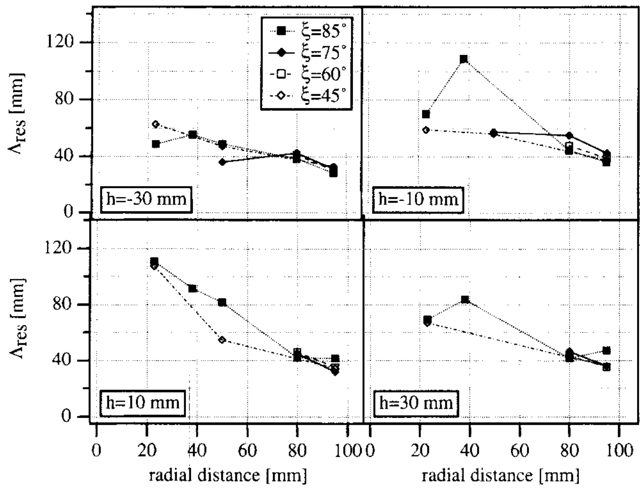

Figure 12. Resultant 3-D length macroscales at $h = -30$ mm and $N = 450$ rpm.

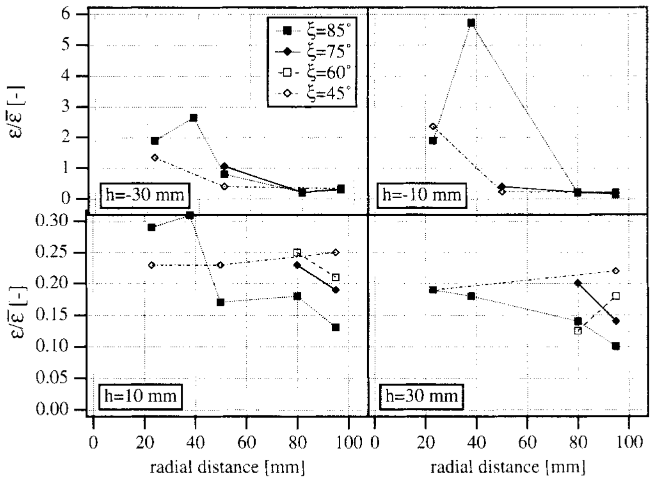

Figure 13. Relative specific energy dissipation rates.
$N = 450$ rpm.

mally in the range 0.01–0.04 m/s. On the other hand, in relative terms, this variation can be as much as 40% of the fluid velocity. At $h = -10$ mm, $r = 38$ mm, $\xi = 85°$, a difference of almost $0.08 \cdot U_{\text{tip}}$ is observed. With a few exceptions, the particles lag behind the fluid when the axial mean velocity component is directed upwards and vice versa, which agrees with findings of Guiraud et al. (1993) and Nouri and Whitelaw (1992). In the baffle region at $h = -30$, $h = 10$, and $h = 30$ mm, there is a tendency for the difference in $|\overline{U}_s - \overline{U}_p|$ to decrease with increasing impeller speed. At $h = 30$ mm, in the baffle region, the process particles occasionally (at a few locations and impeller speeds) have a higher mean velocity than the fluid. Even though the difference in mean velocity at certain measurement points scale with impeller speed, this is not the case in general. The difference in axial mean velocity $|\bar{u}_{h,s} - \bar{u}_{h,p}|$ range from less than 0.01 to 0.04 m/s except for in the discharge flow ($r = 23$ and 38) at $h = -10$ and -30 mm, where values between 0.05 and 0.11 m/s are obtained. The largest difference in the axial mean velocity is approximately $0.04 \times U_{\text{tip}}$ and is found at $h = -10$ mm, $r = 38$ mm, $\xi = 85°$. Concerning the radial mean velocity, the fluid frequently lag behind the particles, but with a difference mostly less than 0.01 m/s. Below the impeller, except for in the discharge flow ($r = 23$, 38 mm) at $h = -10$ mm, the difference in radial mean velocity is lower than the difference in axial mean velocity. The maximum difference in radial mean velocity is $0.04 \times U_{\text{tip}}$ and is found at $h = -10$ mm, $r = 38$ mm, $\xi = 85°$. The difference in tangential mean velocity is in general slightly lower than the difference in axial mean velocity, but is larger than the difference in radial mean velocity. However, the maximum difference of $0.11 \times U_{\text{tip}}$ found in this work is for the tangential component at $h = -10$ mm, $r = 38$ mm, $\xi = 85°$. Hence, our results are not in agreement with the conclusion for a propeller (Guiraud et al., 1993) that the velocities of both phases are equal in the discharge region.

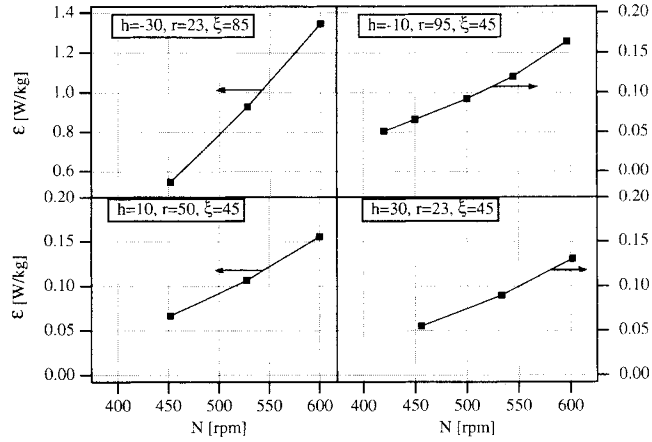

Figure 14. Influence of impeller speed on specific energy dissipation rate.

Based on the mean velocity components, three different flow angles have been defined (Figure 15). α and β are the angles to the vertical axis of the projection of the 3-D velocity vector in the plane formed by the axial-tangential and the

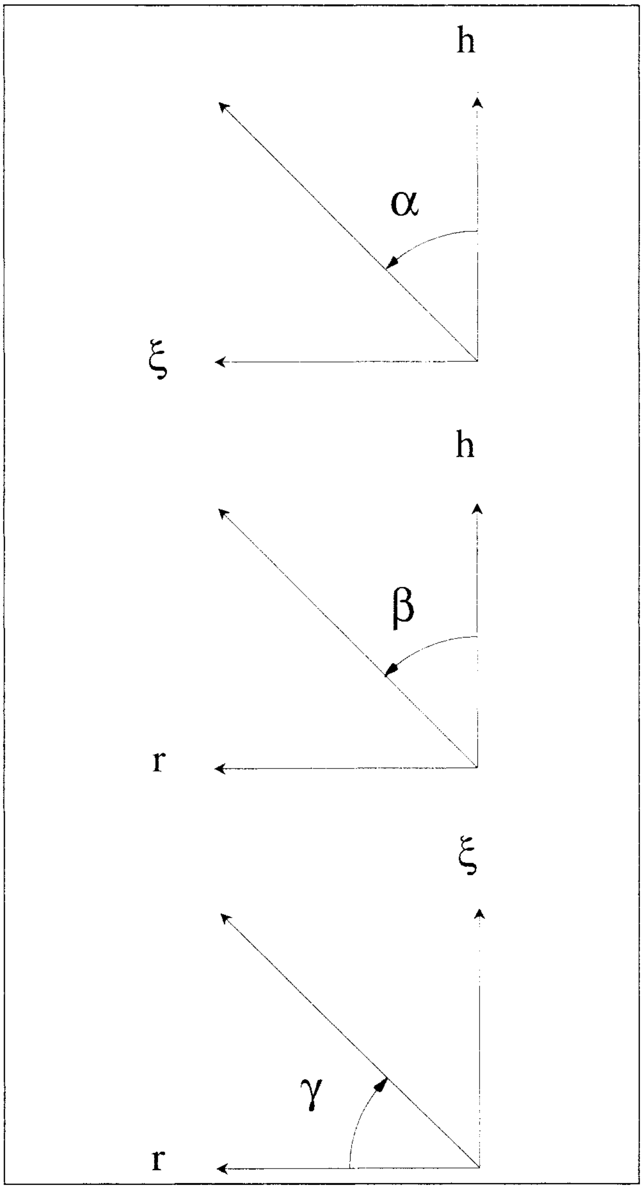

Figure 15. Definition of flow angles.

Table 4. Differences in Mean Velocity Direction of Fluid and Process Particles (deg)

Location	Component	N (rpm)		
		450	525	600
$h=-30,\ r=50,\ \xi=45$	γ	42	24	30
$h=-30,\ r=50,\ \xi=75$	γ	14	13	14
$h=-30,\ r=50,\ \xi=85$	γ	20	21	24
$h=-10,\ r=50,\ \xi=45$	γ	14	18	7
$h=-10,\ r=50,\ \xi=75$	α	15	12	10
$h=10,\ r=50,\ \xi=85$	α	17	13	10
$h=-30,\ r=80,\ \xi=60$	β	19	13	17
$h=-30,\ r=80,\ \xi=60$	γ	10	10	18
$h=10,\ r=80,\ \xi=60$	β	20	13	19
$h=10,\ r=80,\ \xi=60$	γ	20	17	5
$h=10,\ r=80,\ \xi=75$	γ	14	14	3

axial-radial velocity vectors, respectively, and γ is the angle to the radial axis formed by the projection in the radial-tangential plane. The difference in flow angles between the fluid and the process particles are normally less than 10° and mostly much smaller. Two different regions are found where the difference in at least one of the flow angles is higher. The first is in the discharge flow at $h=-10$ mm. At a radial distance of 23 mm, the difference in γ is between 10 and 15°, and at $r=38$ mm the difference in all three angles is around 20°. At $h=-30$ mm, these differences are reduced to below 10°. The second region is at the radial distances of $r=50$ and 80 mm, characterized by low mean velocities. For the latter region, results are given in Table 4 for cases where the difference in flow angles between the two phases exceeds 10% for at least one impeller speed.

The total fluctuating velocity $u'_{i,\mathrm{rms}}$ is almost exclusively higher for the fluid than for the process particles, but the difference is usually small in absolute values, mostly less than 0.03 m/s. In relative terms on the other hand, this can correspond to as much as 20% of the fluid fluctuation. The difference in the 3-D fluctuating velocity ($\sqrt{2q}$, based on the total velocity fluctuations) is approximately 0.01–0.02 m/s except for the region surrounding the impeller (Table 5). Close to the impeller in the discharge flow, differences as large as 0.2 m/s are observed. The difference in fluctuating velocity does not scale with impeller speed.

Discussion

In this work the complete 3-D velocity vector of the fluid is determined directly by a 3-D PDA system. This allows us to use the 3-D velocity for velocity bias correction. In the case of complex 3-D flows, bias correction based on 1-D or 2-D measurements usually introduce errors that are larger than the velocity bias itself (Pettersson, 1996). Direct determination of the complete 3-D velocity vector also allows us to determine all components of the Reynolds stress tensor. Occasionally, the velocity profiles in three dimensions and corresponding turbulence data have been previously reported. However, these results are based on repeated measurements by 1-D or 2-D LDA systems and cannot replace the actual 3-D measurements. First, it is difficult to actually reach the same location in two different measurements from different angles, partly because of wall refraction. Secondly, in a true 3-D measurement the measurement volume is the cross-section volume of two perpendicular (in our case) and strongly elongated ("cigar-shaped") spheroids (see Table 1). However, the measurement volume in 1-D or 2-D is usually the strongly elongated spheroid itself. Hence, in repeated 1-D or 2-D measurements at the same location but from different angles, in order to determine all three velocity components, the measurement volume can, at best, only coincide to a small extent. Especially in the impeller region, this is of importance. In addition, it is impossible to determine Reynolds stresses by repeated 1-D measurements, and 3 different measurements at the same location are required to obtain all Reynolds stress components if a 2-D LDA is used.

The local, instantaneous 3-D velocity of the fluid and of suspended particles have been measured simultaneously. Fluid tracer particles are distinguished from process particles by *in-situ* size determination. The seed particles are small and spherical, and the high reflecting metal coating makes it possible to extend the normal size range of the measurement. However, the density of the particles is high. If the response time of the seed particle (that is, the time for a particle at rest to accelerate to 63% of the fluid velocity (Hetsroni, 1989)) is of the same order of magnitude or longer than the characteristic time scale of the eddies, the fluid motion will not be well represented by the seeds. For particle Reynolds number (based on slip velocity and fluid-particle density difference) below unity, the response time can be calculated as

$$t^* = \frac{d^2\rho_{\mathrm{part}}}{18\mu_f} \tag{20}$$

For the metallic coated particles, the response time estimates to 2 μs. Near the impeller in a stirred tank, the dissipation time scale (a measure of the most rapid changes in the fluctuations of u' (Hinze, 1975)) is of the order of some milliseconds (Costes and Couderc, 1988; Wu and Patterson, 1989). This indicates that the seed particles are acceptable as fluid tracers in spite of the high density. In addition, the seed particles have been compared experimentally with neutral buoyant nylon particles ($d=4$ μm, $\rho_p=1.02$ g/cm^3). Nylon particles are added to the water and the 3-D velocity is measured

Table 5. Differences in the Total Fluctuating Velocity Between the Two Phases

h	r				
	23	38	50	80	85
30	0.012–0.015	0.020–0.026		0.010–0.018	0.010–0.021
10	0.040–0.052	0.035–0.048	0.010–0.019	0.010–0.021	0.011–0.022
−10	0.09–0.15	0.16–0.19	0.010–0.013	< 0.015	< 0.015
−30	0.033–0.053	0.037–0.040	0.040–0.050	0.010–0.021	0.008–0.017

in the discharge flow ($h = -12$ mm). The photomultiplier voltage is then reduced so that the nylon particles become almost nondetectable, and the data rate decreases to 3 Hz. Then, the metallic coated seed particles are added to the fluid. Their ability to scatter light is much stronger, and they are hence detectable also at the low photomultiplier voltage. The data rate increases to about 150 Hz, and the 3-D velocity is measured again. The difference between the nylon and the metallic-coated particles with respect to mean and rms-fluctuating velocities of all three velocity components is within the experimental uncertainty (Pettersson, 1996). This supports that the metallic-coated particles are suitable enough for tracing the fluid flow.

Seed and process particles may influence on the fluid turbulence. Small particles are known to decrease the turbulence intensity, while large particles have been found to increase the turbulence as a result of vortex shedding. Based on experimental data, Gore and Crowe (1989) found the transition to take place when the particle size exceeded approximately 10% of the characteristic length of the most energetic eddies. In our work, the smallest measured macroscale of turbulence is about 10 mm (see Figures 10–12). On the average, our process particles are 321 μm which means that in our system both seed particles and process particles should reduce the level of turbulence. According to Hetsroni (1989), no vortex shedding occurs downstream the particle when

$$Re_p = \frac{d(u_f - u_{\text{part}})}{\nu_f} \leq 110 \tag{21}$$

For the process particles, the Reynolds number is below 110 if the relative velocity is below 0.34 m/s. As described above, the difference in mean velocity between the fluid and the process particles is lower or much lower than this. Of course, the mean velocity difference does not represent the instantaneous actual relative velocity. However, it seems reasonable to conclude that the condition of vortex shedding also suggests that the process particles tend to decrease the level of fluid turbulence. The ratio of seed particle mass to the fluid mass is about 10^{-5}, and for the process particles the ratio is about 0.0015. The magnitude of the influence on the fluid turbulence intensity can be roughly estimated as (Yarin and Hetsroni, 1994)

$$\sigma = \frac{\gamma_m}{1 + \gamma_m} \tag{22}$$

Hence, the results presented for the fluid phase can be interpreted as representing the behavior of a homogeneous fluid phase.

Between 0.15 and 0.3 million data recordings are collected in each measurement as required for estimation of autocorrelation coefficients and in order to collect a sufficient number of process particles. High up in the tank process, particle concentration and flow rate are both low which leads to very long measurement times in order to collect a sufficient number of process particles. This is the main reason for why measurement locations are limited to the lower half of the tank. An increased mean concentration of process particles increases the disturbance of the light beams. An increased seed particle concentration will increase the tendency for two particles to be recorded simultaneously. The receiving optics and the 2-D probe receive scattered light from a certain volume, and in our study the concentration of seed particles corresponds to approximately one particle per two such volumes. The effects of distortion of laser beams in vessel walls have been extensively analyzed (Pettersson, 1996). In the measurements of the present study, such effects can be neglected.

The slot width of 2 milliseconds should not be increased. At 600 rpm, the periodicity of the impeller blades is 25 milliseconds, and the shortest time macroscales are below 15 milliseconds. Sometimes, the autocorrelation coefficients of the present work do not reach zero until a lag time of several seconds. In most of these cases, but not all, a low-amplitude periodicity of about a second is present. Usually, this principal shape of the autocorrelation coefficient curve is essentially unchanged when the agitation rate is altered. Random noise in the system does not influence on the numerator of $R_E(\tau)$ (Absil, 1988), but will increase the denominator, which increases the rate of decay of the autocorrelation coefficient. In addition, the behavior is only found in some cases and is hence not likely to be systematic deficiency of the measurement technique. Neither does the problem originate from the bias correlation applied in this work, since similar results are obtained if the fluctuating velocities are based on uncorrected mean velocities and a weighting factor of unity instead of $1/U$ in Eq. 11. Detailed data about the autocorrelation coefficients are rarely given in the literature. However, autocorrelation coefficients that fluctuate with the same frequency as the passage of the impeller blades, but with a decaying amplitude, are in accordance with data presented by Mahouast et al. (1989). In the present study, the amplitude of the fluctuation is increasing with decreasing distance to the impeller, and this corresponds to results of Mujumdar et al. (1970) and Rao and Brodkey (1972). The longer periodicity in the order of a second found in this work has also been reported by Kresta and Wood (1993a) for a pitched blade turbine. Low-frequency oscillations may relate to the fluctuations in the macroscale flow pattern that are reported by Bruha et al. (1995) for axial flow turbines and by Winardi and Nagase (1991) for a propeller. According to Winardi and Nagase (1991), the macroscale flow pattern is far from stable. It fluctuates between two different basic patterns with different intermediate patterns. In each moment the flow pattern is different in the different baffle sectors. Haam et al. (1992) related low-frequency oscillations in heat-transfer coefficients to vortices at the surface that were observed to slowly rotate around the impeller axis. In the present work, we have visually observed that clouds of process particles sweep through the tank now and then. A detailed examination of the origin of nonstandard behaviors of the autocorrelation coefficients is outside the scope of this study. However, the shape of the autocorrelation coefficient curves affects the estimation of the periodic velocity fluctuation generated by the impeller blades and the estimation of time macroscales and, hence, of energy dissipation rates. The uncertainty in the periodic rms fluctuating velocity is normally about 0.02 m/s or less, as estimated by comparison of values obtained from different lag time periods. However, sometimes and especially in the radial component at $h = -10$ mm, the uncertainty is higher and in a few cases much higher. The uncertainty in

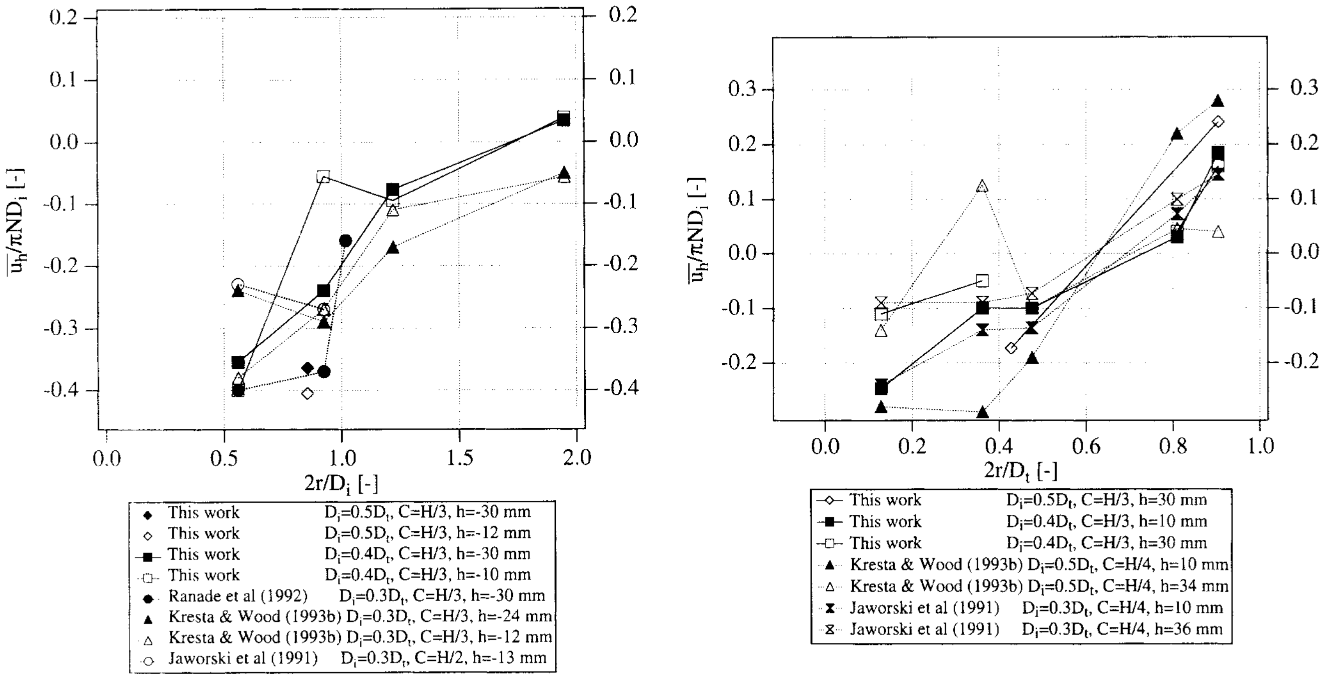

Figure 16. Comparison of mean velocities with literature data.

time macroscales is 10 to 15% for well-shaped autocorrelation coefficient curves, and it is encouraging to find that the local energy dissipation rate depends on the agitation rate to power approximately three in these cases. For autocorrelation coefficients retaining a periodicity from the impeller blades, the uncertainty in the estimated time macroscales increases up to 50%.

Literature data on axial mean velocities are compared with the data of the present study in Figure 16. The location of the measurement points are not always exactly the same, but differences in configuration, such as in D_i/D_t and impeller clearance C, are probably more important. Variations in D_i/D_t and C changes the velocity profiles of the discharge flow (Kresta and Wood, 1993b; Ranade and Joshi, 1989), which may explain the differences found below the impeller (left diagram).

The turbulence of the bulk flow in a stirred tank is often assumed to be isotropic (such as Jaworski et al. (1991)). This is supported by our results on averaged shear stresses and rms-fluctuating velocities. The shear stresses are very close to zero in the baffle region and fairly close in the rest of the tank, except for in the discharge flow. The variation in rms-fluctuating velocities with flow direction (Figure 5) is frequently 30% or more, which is larger than the statistical uncertainty. However, the differences in absolute values are small, between 0.04 and 0.07 m/s, and rms-fluctuating velocities are sensitive to noise within the Doppler system (Absil, 1988). An isotropic bulk flow, therefore, seems to be an acceptable assumption. However, concerning the discharge flow our results show that in this region the turbulence should not be assumed to be isotropic.

Conclusions

Direct measurements of the complete local 3-D velocity vectors of the fluid flow and of suspended process particles in a tank agitated by a pitched-blade turbine are reported. The overall flow pattern is as expected and does not change with agitation rate. The 3-D mean and total fluctuating velocities of the fluid are proportional to the impeller tip speed. The flow around the impeller is more complex than expected. Tangential mean flow opposite to the impeller rotation is found outside and above the impeller. Impeller fluctuations are also found above the impeller and results indicate that the baffle disturbs the flow around the impeller. Significant spatial variations in the outflow are consistent with the presence of a high speed jet. After subtraction of the impeller periodicity, a decaying periodic fluctuation sometimes remains in the autocorrelation curves, and a longer periodicity of one to two seconds is occasionally observed. The bulk of the tank can be considered to be isotropic. The discharge flow is characterized by higher turbulent kinetic energies, total Reynolds stresses and energy dissipation rates, and differences are found depending on the coordinate direction. As expected, the total normal stresses are in general larger than the corresponding shear stresses, especially below the impeller. The time macroscales are essentially independent of impeller speed. 1-D length macroscales are different in different directions and vary with one order of magnitude with location. Tangential gradients are found below the impeller and in the baffle region. Local energy dissipation rates scale with impeller speed raised to power three. The difference in the 3-D mean velocity of the fluid and of the process particles, respectively, show a complex dependence on location and impeller speed. It cannot be claimed that the difference in one particular velocity component, in general, is more dominating than any other. Differences in mean and fluctuating velocities between the two phases are often small, but increase in the discharge flow. Also found in this region, and in the region characterized by low mean velocities, are differences in mean velocity direction of the two phases.

Notation

a_0, a_1, a_2 = coefficients obtained from curve fitting
C = impeller clearance to tank bottom, m
C_k = constant in Eq. 18
d = particle diameter, m
D_i = impeller diameter, m
D_t = tank diameter, m
h = axial direction, m
H = liquid height in tank, m
k_1, k_2, k_3 = empirical regression parameters
N_{part} = number of particles in measurement, #
N_p = power number
N = impeller speed, rps
P = power, W
Re_p = particle Reynolds number defined in Eq. 21
t = time, s
T_E = time macroscale, m
U_c = convection velocity, m/s
U_{tip} = impeller tip speed, m/s
V = volume, m^3
α, β, γ = flow angles, deg
ϵ = turbulent energy dissipation rate, W/kg
γ_m = mass of particles divided by mass of fluid, kg/kg
Λ = length macroscale, m
ν = kinematic viscosity, m^2/s
μ = dynamic viscosity, Ns/m^2
ρ = density, kg/m^3
σ = relative change in turbulence intensity due to the presence of particles, %
τ = lag time, s
$\overline{\quad}$ = mean value

Subscripts

f = of the fluid
h = axial component
i, j, k = arbitrary coordinate directions
p = process particles
part = particle
per = periodic
r = radial component
res = resultant
s = seed particles
turb = random
ξ = tangential component

Literature Cited

Absil, L. H. J., "Laser-Doppler Measurements of Mean Turbulence Quantities, Time- and Spatial-Correlation Coefficients in the Wake of a Circular Cylinder," *Int. Symp. on Laser-Doppler Anemometry to Fluid Mechanics*, Lisbon, Portugal, p. 45 (1988).

Ali, A. M., H. H. S. Yuan, D. S. Dickey, and G. B. Tatterson, "Liquid Dispersion Mechanisms in Agitated Tanks. I. Pitched Blade Turbine," *Chem. Eng. Commun.*, **10**(4–5), 205 (1981).

Armstrong, S. G., and S. Ruszkowski, "The Flow Field in the Discharge Stream of Disk Turbines," Eur. Conf. on Mixing, BHRA, Cranfield, Bedford, U.K., p. 1 (1988).

Bakker, A., and H. E. A. van den Akker, "Single-Phase Flow in Stirred Reactors," *Trans. Inst. Chem. Engrs.*, **72**, A(7), 583 (1994).

Bates, R. L., P. L. Fondy, and R. R. Corpstein, "An Examination of Some Geometric Parameters of Impeller Power," *I.E.C. Proc. Des. Dev.*, **2**(4), 310 (1963).

Baukhage, K., "The Phase-Doppler-Difference-Method, a New Laser-Doppler Technique for Simultaneous Size and Velocity Measurements," *Part. Part. Syst. Charact.*, **5**, 16 (1988).

Bruha, O., I. Fort, and P. Smolka, "Phenomenon of Turbulent Macro-Instabilities in Agitated Systems," *Collect. Czech. Chem. Commun.*, **60**(1), 85 (1995).

Calabrese, R. V., and C. M. Stoots, "Flow in the Impeller Region of a Stirred Tank," *Chem. Eng. Prog.*, **85**(5), 43 (1989).

Costes, J., and Couderc, J. P., "Study by Laser-Doppler Anemometry of the Turbulent Flow Induced by a Rushton Turbine in a Stirred Tank: Influence of the Size of the Units: II. Spectral Analysis and Scales of Turbulence," *Chem. Eng. Sci.*, **43**(10), 2765 (1988).

Fort, I., R. Neugebauer, and M. Pasturikova, "Studies on Mixing: XXIX. Spacial Distribution of Mechanical Energy Dissipated by Axial Mixer in a System with Radial Baffles," *Collect. Czech. Chem. Commun.*, **36**, 1769 (1971).

Gore, R. A., and C. T. Crowe, "Effect of Particle Size on Modulating Turbulent Intensity," *Int. J. Multiphase Flow*, **15**(2), 279 (1989).

Guiraud, P., T. Paul, J. Bertrand, and J. Costes, "Particle and Liquid Velocities Measurements in a Stirred Suspension," *Symp. on Industrial Crystallization*, Z. H. Rojkowski, ed., Warsaw, Polen, p. 4-179 (1993).

Günkel, A. A., and M. E. Weber, "Flow Phenomena in Stirred Tanks," *AIChE J.*, **21**(5), 931 (1975).

Haam, S., R. S. Brodkey, and J. B. Fasano, "Local Heat Transfer in a Mixing Vessel Using Heat Flux Sensors," *Ind. Eng. Chem. Res.*, **31**(5), 1384 (1992).

Hetsroni, G., "Particles-Turbulence Interaction," *Int J. Multiphase Flow*, **15**(5), 735 (1989).

Hinze, J. O., *Turbulence*, 2nd ed., McGraw-Hill, New York (1975).

Ito, S., K. Ogawa, and N. Yoshida, "Turbulence in Impeller Stream in a Stirred Vessel," *J. Chem. Eng. Jpn.*, **8**(3), 206 (1975).

Jaworski, Z., and I. Fort, "Energy Dissipation Rate in a Baffled Vessel with Pitched Blade Turbine Impeller," *Coll. Czech. Chem. Commun.*, **56**(9), 1856 (1991).

Jaworski, Z., I. Fort, and F. Strek, "Turbulent Flow Characteristics for Pitched Blade Turbine," *Collect. Czech. Chem. Commun.*, **53**(5), 957 (1988).

Jaworski, Z., A. W. Nienow, E. Koutsakos, K. Dyster, and W. Bujalski, "An LDA Study of Turbulent Flow in a Baffled Vessel Agitated by a Pitched Blade Turbine," *Trans. Inst. Chem. Eng. Part A*, **69**, 313 (July, 1991).

Kresta, S. M., and P. E. Wood, "The Flow Field Produced by a PBT: Characterization of the Turbulence and Estimation of the Dissipation Rate," *Chem. Eng. Sci.*, **48**(10), 1761 (1993a).

Kresta, S. M., and P. E. Wood, "The Mean Flow Field Produced by a 45° PBT: Changes on the Circulation Pattern Due to Off Bottom Clearance," *Can. J. Chem. Eng.*, **71**, 42 (1993b).

Kuboi, R., I. Komasawa, and T. Otake, "Fluid and Particle Motion in Turbulent Dispersion," *Chem. Eng. Sci.*, **29**, 651 (1974).

Mahouast, M., G. Cognet, and R. David, "Two-Component LDV Measurements in a Stirred Tank," *AIChE J.*, **35**(11), 1770 (1989).

Mayo, W. T., Jr., M. T. Shay, and S. Riter, "Digital Estimation of Turbulence Power Spectra from Burst Counter LDV Data," *Proc. II Int. Workshop on Laser Velocimetry*, H. D. Thompson and W. H. Stevenson, eds., Purdue Univ., p. 16 (1974).

Mujumdar, A. S., B. Huang, D. Wolf, M. E. Weber, and W. J. M. Douglas, "Turbulence Parameters in a Stirred Tank," *Can. J. Chem. Eng.*, **48**, 475 (1970).

Nouri, J. M., and J. H. Whitelaw, "Particle Velocity Characteristics of Dilute to Moderately Dense Suspension Flows in Stirred Reactors," *Int. J. Multiphase Flow*, **18**(1), 21 (1992).

Nouri, J. M., and J. H. Whitelaw, "Flow Characteristics of Stirred Reactors with Newtonian and non-Newtonian Fluids," *AIChE J.*, **36**(4), 627 (1990).

Oldshue, J. Y., *Fluid Mixing Technology*, McGraw-Hill, New York (1983).

Pettersson, M., "Application of Three-Dimensional Phase Doppler Anemometry to Stirred Suspension Hydrodynamics," PhD Thesis, Dept. of Chemical Engineering and Technology, Royal Inst. of Technology, Stockholm, Sweden (1996).

Raghav Rao, K. S. M. S., and J. B. Joshi, "Liquid Phase Mixing in Mechanically Agitated Vessels," *Chem. Eng. Commun.*, **74**, 1 (1988).

Ranade, V. V., and J. B. Joshi, "Flow Generated by Pitched Blade Turbines: 1. Measurements Using LDA," *Chem. Eng. Commun.*, **81**, 197 (1989).

Ranade, V. V., V. P. Mishra, V. S. Saraph, G. B. Deshpande, and J. B. Joshi, "Comparison of Axial Flow Impellers Using LDA," *Ind. Eng. Chem. Res.*, **31**, 2370 (1992).

Rao, M. A., and R. S. Brodkey, "Continuous Flow Stirred Tank Turbulence Parameters in the Impeller Stream," *Chem. Eng. Sci.*, **27**, 137 (1972).

Rewatkar, V. B., K. S. M. S. Raghav Rao, and J. B. Joshi, "Power

Consumption in Mechanically Agitated Contactors Using PBT Impellers," *Chem. Eng. Commun.*, **88**, 69 (1990).

Rewatkar, V. B., and J. B. Joshi, "Effect of Impeller Design on Liquid Phase Mixing in Mechanically Agitated Reactors," *Chem. Eng. Commun.*, **102**, 1 (1991).

van't Riet, K., W. Bruijn, and J. M. Smith, "Real and Pseudo-Turbulence in the Discharge Stream from a Rushton Turbine," *Chem. Eng. Sci.*, **31**, 407 (1976).

Shiue, S. J., and C. W. Wong, "Studies on Homogenization Efficiency of Various Agitators in Liquid Blending," *Can. J. Chem. Eng.*, **62**, 602 (1984).

Stoots, C. M., and R. V. Calabrese, "Mean Velocity Field Relative to a Rushton Turbine Blade," *AIChE J.*, **41**(1), 1 (1995).

Tatterson, G. B., H. H. S. Yuan, and R. S. Brodkey, "Stereoscopic Visualization of the Flows for Pitched Blade Turbines," *Chem. Eng. Sci.*, **35**, 1369 (1981).

Townsend, A. A., *The Structure of Turbulent Shear Flow*, Cambridge University Press, London, UK, p. 18 (1976).

Winardi, S., and Y. Nagase, "Unstable Phenomenon of Flow in a Mixing Vessel with a Marine Propeller," *J. Chem. Eng. Japan*, **24**(2), 243 (1991).

Wu, H., and G. K. Patterson, "Laser-Doppler Measurements of Turbulent-Flow Parameters in a Stirred Mixer," *Chem. Eng. Sci.*, **44**(10), 2207 (1989).

Yarin, L. P., and G. Hetsroni, "Turbulence Intensity in Dilute Two-Phase Flows: 3. The Particles-Turbulence Interaction in Dilute Two-Phase Flow," *Int. J. Multiphase Flow*, **20**(1), 27 (1994).

Zwietering, Th. N., "Suspending of Solid Particles in Liquid by Agitators," *Chem. Eng. Sci.*, **8**, 244 (1958).

Manuscript received Feb. 11, 1997, and revision received Oct. 6, 1997.